

# Anomalous Dynamics of a Liquid Corner Film

Marcel Moura<sup>1</sup>, Vanessa Kern<sup>2</sup>, Knut Jørgen Måløy<sup>1,3</sup>, Andreas Carlson<sup>2</sup>, and Eirik G. Flekkøy<sup>\*1,4</sup>

<sup>1</sup>PoreLab, Department of Physics, University of Oslo, NO-0316 Oslo, Norway

<sup>2</sup>Department of Mathematics, University of Oslo, NO-0316 Oslo, Norway

<sup>3</sup>PoreLab, Department of Geoscience and Petroleum, Norwegian University of Science and Technology, NO-7031 Trondheim, Norway

<sup>4</sup>PoreLab, Department of Chemistry, Norwegian University of Science and Technology, NO-7491 Trondheim, Norway

January 27, 2025

## Abstract

Measuring the rheology of liquids typically requires precise control over shear rates and stresses. However, we demonstrate that the features of a power-law fluid can be predicted by simply observing the capillary spreading dynamics of viscous droplets within a wedge-shaped geometry. By considering the influence of capillary and viscous forces within this geometry, we show that the spreading dynamics can be described by a nonlinear diffusion equation. Analytical predictions indicate subdiffusive behavior, establishing a direct relationship between the diffusion exponent and the rheological exponent, which is also corroborated by experimental results. Since this relationship is independent of flow details, it provides robust predictions for the rheological properties of power-law fluids.

## 1 Introduction

The spreading of droplets on solid surfaces is an ubiquitous phenomenon that may be observed when rain falls on a window, as well as in a range of biological, geological and physical systems where it may be the mechanism that provides nutrition to living cells [1], oxidating substances to minerals [2] or fluid pathways inside other complex geometries [3, 4]. The spontaneous spreading of fluids depends on the wetting properties and geometry of the medium through which it spreads [5, 6, 7, 8, 9]. However, it also depends crucially on the rheology of the liquid, as is well known from the everyday application of non-Newtonian fluids, such as toothpaste, corn starch, paint, yogurt and shampoo. Controlling fluid rheology is also topical in industrial applications and in food science [10, 11, 12, 13, 14, 15, 16] where it covers everything from cooking recipes to consumer satisfaction. In this study, we show that the spreading dynamics of a droplet of a power-law liquid can be used to predict the fluid's rheological properties.

The rheology of a powerlaw fluid is characterized by the fact that the shear stress is given by a power of the strain rate. The spreading of such a liquid in a wedge-shaped geometry is anomalous in the sense that it is described in the same way as anomalous diffusion. Mathematically, it is captured by a nonlinear diffusion equation that yields analytical so-

lutions with a sub-diffusive spreading rate which is given by an anomalous diffusion exponent [17, 18, 19]. As an interesting by-product we obtain a relationship between the exponent governing the rheology and the diffusion exponent. As this relationship depends only on the conservation of fluid mass and a non-linear Darcy law, which relates the volume flux to the pressure gradient, it is independent of other details of the flow structure.

The analysis and findings presented here complement the extensive literature on anomalous diffusion. Pattle [20] noted already in 1959 that the seepage of a liquid into a cloth or porous body could be described by a nonlinear diffusion equation yielding sub-diffusive spreading of the fluid. In the 1980's there was a large effort to understand the nature of anomalous diffusion, in particular in the context of transport in disordered and porous media. In porous media flows, there are many practical situations where a strong level of confinement leads to regimes where the transport occurs through corners and films where the balance between capillary and viscous forces play a key role, some times leading to persistent, long-rang transport [21, 22, 23, 24, 5] as when connecting otherwise disconnected fluid clusters [25, 26, 27, 28, 29, 30, 31, 32, 33].

In this study, we combine the mathematical tools describing anomalous diffusion [20, 18] with the hydrodynamics of non-Newtonian liquids, thus provid-

ing a minimal model that can also be extended to film flows in more complex geometries. The solution pertains to a viscous flow driven by capillarity as a droplet spreads in an idealized (sharp) wedge (see Fig. 1a) with a constant solid-liquid contact angle. By combining theory and experiments we show how the rheological exponent of a power-law fluid may be obtained solely on the basis of the spontaneous, capillary driven, fluid motion, and without any type of force- or shear rate control, as needed in commercial rheometers.

## 2 Theory

A droplet of a power-law fluid spreading in a wedge is characterized by the stress-strain relationship  $\sigma \propto \dot{\gamma}^n$  over a certain range of the strain rate  $\dot{\gamma}$ , which are frequently described by the Ostwald-de Waele model [13]. The viscosity is then given by

$$\mu = \eta_0 \dot{\gamma}^{n-1} = \mu_0 \left( \frac{\dot{\gamma}}{\dot{\gamma}_0} \right)^{n-1} \quad (1)$$

where  $\mu_0$  and  $\mu$  are in units of Pa s, the exponent  $n = 1$  corresponds to a Newtonian fluid and  $\dot{\gamma}_0$  is a reference strain rate at which the liquid is non-Newtonian, we shall take  $\dot{\gamma}_0 = 10 \text{ s}^{-1}$  for the fluids employed in this study (see the rheological characterization of the fluids in the Supplementary Material). Many polymer melts and solutions exhibit a value of  $n$  in the range 0.3-0.7 depending upon the concentration and molecular weight of the polymer [35]. Even smaller values of the power-law exponent ( $n = 0.1-0.15$ ) are encountered with fine particle suspensions like kaolin-in-water, bentonite-in-water, etc. By using polyacrylamide solutions of different concentrations Ansari et al. [36], measured a range of power-law indices  $n = 0.26 - 0.47$ , which were obtained for shear rates in the range  $10 - 1000 \text{ s}^{-1}$ .

We shall obtain a prediction for the height  $h(x, t)$  of a droplet of a power-law fluid when spreading along the wedge geometry, as shown in Fig. 1. Our power-law liquid wets the surface inside the wedge and spreads due to the capillary forces, as illustrated in Fig. 1 a). Its shape is described by the height  $h(x, t)$ . When the wetting angle  $\Theta < (\pi - \alpha)/2$ ,  $\alpha$  being the opening angle of the wedge, the capillary pressure will be negative and the minimal energy will be reached when the solid-liquid contact area is maximized, that is, when the liquid spreads out as far as possible along the wedge.

In the Supplementary Material we show that the volumetric flow rate  $q$  across a surface normal to the corner line may be written

$$q = Q_n \left( \frac{-\partial P / \partial x}{\eta_0} \right)^{1/n} h^{3+1/n}, \quad (2)$$

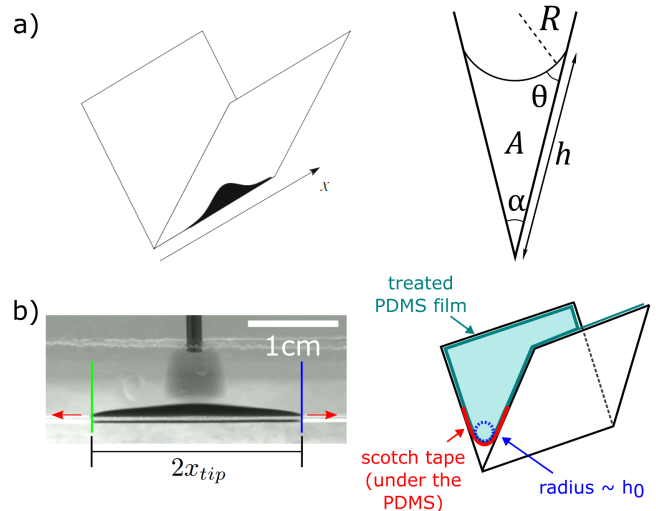


Figure 1: a) Liquid droplet spreading in a wedge. The right sketch shows the cross-sectional area  $A$  and the local height  $h$  of the spreading droplet, which both vary along the wedge. Here,  $\alpha$  is the opening angle of the wedge and  $\Theta$  is the contact angle at the liquid-solid-air contact line. b) On the left we show a snapshot of the experiment where the green and blue vertical lines denote the left and right tip position and the red arrows indicate the spreading direction. The right diagram illustrates the Scotch tape (red) and PDMS layer (cyan) employed which lead to an effective finite radius of curvature  $h_0$  in the corner (exaggerated in the figure for clarity). Note the main difference between the idealized (sharp) wedge and the experimental setup is a finite curvature where the plates meet.

where  $P$  is the capillary pressure,  $x$  is the coordinate along the wedge,  $h(x)$  is the height of the liquid in the normal direction, and

$$Q_n = \frac{2^{\frac{1+n}{2n}} n^2}{(2n+1)(3n+1)} \left( \frac{\alpha}{2} \right)^{\frac{2n+1}{n}} \quad (3)$$

is a dimensionless average of the flow field which is dependent on our choice of flow geometry, but not its length scale.

In order to obtain an analytical solution, our theoretical approach ignores; 1) Dynamic variation of the contact angle  $\Theta$  and pinning effects, 2) The finite initial droplet width and the interface curvature in the  $x$ -direction, 3) The cut-offs in shear rates where the non-Newtonian behavior becomes Newtonian, 4) The finite curvature of the corner geometry.

Despite these simplifications we will show below that the model is still predictive, and these are not limiting the spreading dynamics and compares favorably with experiments. These assumptions are partly justified by small  $h$ -values (gravity effects) and a small Reynolds number (inertial effects). Also, we

will show the influence of finite wedge curvature in our numerical solutions by including a corner curvature through the capillary pressure equal to zero when  $h$  falls below a threshold  $h_0$ , see Fig. 1b). Assuming the contact angle  $\Theta$ , to be constant, approximating it by  $\Theta = 20^\circ$ , the curvature of the liquid interface  $1/R$  sets the capillary pressure difference across this interface

$$P(x) = -\frac{\cos(\Theta + \alpha/2)\sigma}{h(x)\sin(\alpha/2)}. \quad (4)$$

where  $\sigma$  is the liquid-air surface tension and we have applied a simple geometric argument to replace  $R$  by  $h$  and the relevant angles shown in Fig. 1a).

It is the variations in  $h(x)$  that will cause a pressure gradient along the wedge, and we may invoke Eq. (2) to get the mean flow. The cross-sectional area in the direction normal to  $x$ ,  $A(x) = (\alpha/2)h^2$ , and the amount of liquid volume is a conserved quantity so that

$$\frac{\partial A}{\partial t} + \frac{\partial q}{\partial x} = 0. \quad (5)$$

Expressing  $h$  by  $A$  in Eq. (2) and using Eq. (4) the volume conservation may then be written on the form

$$\frac{\partial A}{\partial t} = -D_0 \frac{\partial}{\partial x} \left( A^{3/2-1/n} \left( -\frac{\partial A}{\partial x} \right)^{1/n} \right). \quad (6)$$

where the 'diffusion coefficient'

$$D_0 = \left( \frac{2}{\alpha} \right)^{3/2} \left( \frac{\sigma \cos(\Theta + \alpha/2)}{\eta_0 \sin(\alpha/2)} \right)^{1/n} Q_n \quad (7)$$

has dimensions of  $m^{1/n}/s$ .

Since the solution  $A(x, t)$  is symmetric around  $x = 0$ , we will only consider  $x > 0$ , so that  $\partial P/\partial x < 0$ . By taking the initial condition to be  $A(x, 0) = V_0 \delta(x)$ , where  $V_0$  is the droplet volume, we shall follow [18] and seek a scaling solution of the form

$$A(x, t) = \frac{p(u)}{f(t)} \quad (8)$$

where

$$u = \frac{x}{f(t)}. \quad (9)$$

This solution has the property that  $\int dx A(x, t) = \int du p(u) = V_0$ , where  $V_0$  is the initial fluid volume. In order to insert Eq. (8) in Eq. (6) we need the derivative  $\partial A/\partial t = -(f'(t)/f(t)^2)d(up)/du$ , which allows us to write Eq. (6) in the form

$$\frac{f'(t)}{D_0 f^{-1/2-1/n}} = \frac{(p^{3/2-1/n}(-dp/du)^{1/n})'}{d(up)/du} = \lambda \quad (10)$$

where we have separated the  $u$  and  $t$ -dependent terms with the separation constant  $\lambda$ . Integration of the  $f(t)$ -part of Eq. (10) is straightforward and yields

$$f(t) = \left( \frac{\lambda D_0 t}{\tau} \right)^\tau \quad (11)$$

with

$$\tau = \frac{2n}{2+3n}. \quad (12)$$

The  $p$ -part of Eq. (10) takes the form  $(d/du)(p^{3/2-1/n}(-dp/du)^{1/n}) - \lambda up = 0$  which may be integrated to give  $p^{3/2-1/n}(-p'(u))^{1/n} - \lambda up = K$ . Since, by symmetry  $p'(0) = 0$  and  $p(0)$  must be finite, the integration constant  $K = 0$ , and the above equation may be rearranged to give  $p^{n/2-1}p' = -\lambda^n u^n$ , which may be integrated to give

$$p(u) = \lambda^2 \left( \frac{n}{2(n+1)} \right)^{2/n} (L^{n+1} - u^{n+1})^{2/n}, \quad (13)$$

where the normalization condition yields the integration constant  $L = \lambda^{-\tau}(V_0/A_n)^{\tau/2}$  with  $A_n = 2(n/(2(n+1)))^{2/n} \int_0^1 dy (1-y^{n+1})^{2/n}$ . Inserting this  $L$ -value in  $A(x, t) = p(u)/f(t)$ ,  $\lambda$  cancels out, and so we are free to choose  $\lambda = \dot{\gamma}_0/D_0$  in order to make

$$f(t) = \left( \frac{\dot{\gamma}_0 t}{\tau} \right)^\tau \quad (14)$$

dimensionless. Then  $L(D_0) = ((D_0/\dot{\gamma}_0)(V_0/A_n)^{1/2})^\tau$ , and  $u$  gets the dimension of  $m$  and  $p(u)$   $m^2$ . Inserting  $\lambda$  in Eq. (13) finally yields

$$p(u) = \left( \frac{\dot{\gamma}_0}{D_0} \right)^2 \left( \frac{n}{2(n+1)} \right)^{2/n} (L^{n+1}(D_0) - u^{n+1})^{2/n}. \quad (15)$$

Requiring that  $p(u)$  be real restricts this solution to the  $x$ -domain where  $L^{n+1} - u^{n+1} > 0$ , or  $|u| < L$ . Outside

$$x_{tip}(t) = Lf(t) = \left( \left( \frac{V_0}{A_n} \right)^{1/2} \frac{D_0 t}{\tau} \right)^\tau \quad (16)$$

$A(x, t)$  then vanishes exactly, so that  $2x_{tip}(t)$  is the extent of the droplet.

The fact that  $x_{tip} \propto t^\tau$  is a key result as it provides the link between the spreading rate and the diffusion exponent  $\tau$ , and by Eq. (12), the rheological exponent  $n$ . The  $\tau$ -exponent is simply obtained by plotting the experimental  $x_{tip}(t)$ -values on a log-log plot. Having obtained the  $\tau$  and  $n$ -values from  $x_{tip}(t)$  in this way, the scaling function  $f(t)$  is known and may be used to obtain a data-collapse for the experimental values of  $A(x, t)f(t)$  versus  $x/f(t)$  as predicted by theory. With this experimental data-collapse fitting Eq. (15) to the data using  $D_0$  as a fitting parameter gives  $D_0$ . The rheological prefactor  $\mu_0$  may then in principle be obtained by solving Eq. (7) with respect  $\mu_0 = \eta_0 \dot{\gamma}_0^{n-1}$

$$\mu_0 = \left( \frac{2}{\alpha} \right)^{3n/2} \frac{\sigma \cos(\Theta + \alpha/2)}{2 \sin(\alpha/2)} \left( \frac{Q_n}{D_0} \right)^n \dot{\gamma}_0^{n-1}, \quad (17)$$

provided a constant contact angle. However, as is well known, the static contact angle, which we measure to be  $\Theta \approx \pi/9$ . will in general be replaced

by a dynamic contact angle  $\Theta_{dyn}$  once the contact line is moving: Hoffmann [37] showed that the difference between  $\Theta_{dyn}$  and  $\Theta$  is governed by the local capillary number  $Ca$  via a general scaling relation. Later, Sheng [38] and Kokko-Latva and Rothmann [39] showed that this relation is well approximated by  $\cos(\Theta) - \cos(\Theta_{dyn}) \propto Ca$  with a prefactor of order unity. The capillary number  $Ca$  is the ratio of viscous to capillary forces, so in our case  $Ca \sim 1$ , since these are the dominating forces that govern the flow, in particular close to  $x_{tip}$ .

Also, since the analytic theory ignores the corner curvature  $h_0$ , an experimentally measured value of  $h(x, t)$  (the distance from the curved corner to the meniscus) will be associated with an overestimated value of the capillary pressure that drives the flow. This will predict a faster overall spreading rate than what is actually observed. This effect thus has the opposite effect of the dynamic contact angle increasing above the static one, which will lead to a slower spreading.

For these reasons  $\mu_0$  cannot be obtained from Eq. (17) unless  $\Theta_{dyn}$  is measured independently and used instead of  $\Theta$ , and the corner made sufficiently sharp.

### 3 Experimental results and comparison

The mathematical model can be solved numerically, where the solutions provide testable predictions. To test these predictions, we design an experimental system consisting of two thin transparent plates, arranged at an angle  $\alpha = 30^\circ$  and securely held by a support mechanism (see Fig. 1). Standard microscope glass slides (dimensions 76mm  $\times$  26mm  $\times$  1mm) were used. One critical experimental aspect was to ensure a high level of wettability with the wedge and minimize impurities that may affect the contact line motion. As such, the plates were coated with a thin polymeric layer of PDMS, modified with a hydrophilic agent (methyl-terminated poly(dimethylsiloxane-b-ethylene oxide)). The coating was further treated with nitrogen plasma to enhance the wettability, for further details see the Supplementary Material. We tested a range of different fluids, including mixtures of xanthan gum (XG) and water at varying concentrations, as well as a glycerol-water mixture to represent the Newtonian case. The XG concentration in water was systematically varied from 0.5g/L to 6g/L.

In the experiment the initial half-width of the droplet  $w_0 \sim 1$  mm and the wedge's corner is not infinitely sharp, rather it has a radius of curvature  $h_0 \approx 0.6$  mm due to the finite thickness of the PDMS

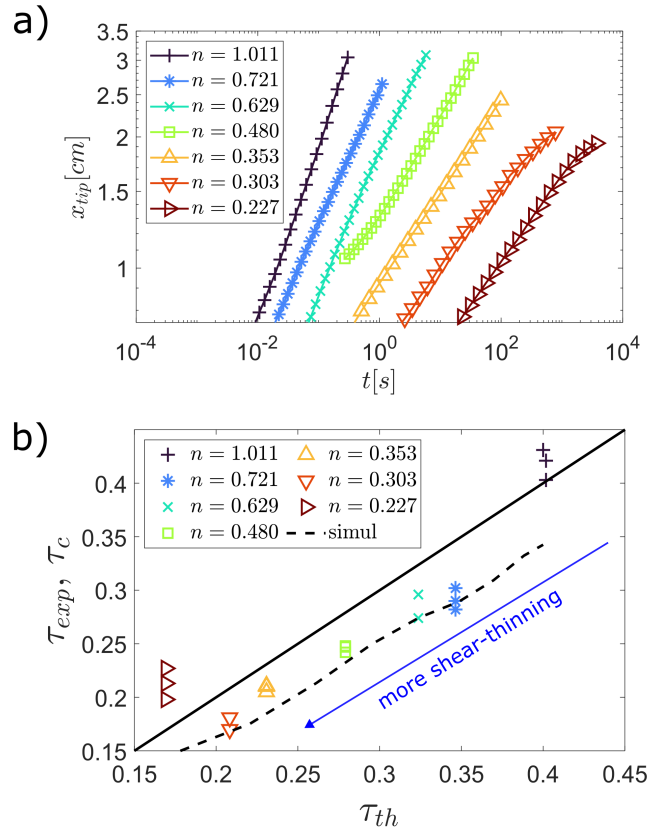


Figure 2: a) Experimentally measured droplet spread  $x_{tip}(t)$ . The curves are shifted horizontally by arbitrary values to aid visualization. The leftmost curve corresponds to the Newtonian fluid while the others are from XG fluids with XG concentrations of 0.5, 1, 2, 3, 4 and 6 g/L increasing from left to right. b) Comparison between the experimental exponent  $\tau_{exp}$  (symbols) and numerical exponent  $\tau_c$  (dashed line), as well as the theoretical slopes  $\tau_{th}$  computed from Eq. (12) (full line). The numerical results take the finite corner curvature  $h_0 = 0.6$  mm and initial profile width  $w_0 = 0.8$  mm into account.

coating, see Fig. 1 b). To mimic the experiments, we solve Eq. (5) numerically, introducing a Gaussian initial profile for  $h(x, t)$  and a cut-off corresponding to the corner curvature. This cut-off arises because the capillary pressure changes sign approximately at the point where  $h(x, t)$  becomes smaller than  $h_0$ , see Fig. 1 a). We set  $h_0 = 0.6$  mm and  $w_0 = 0.8$  mm throughout in the numerical calculations, similar to the experiments. This may be represented mathematically by imposing  $q = 0$  in Eq. (5) where  $h(x, t) < h_0$ . Eq. (6) can then be integrated numerically using centered spatial derivatives and an explicit first order time stepping scheme.

Fig. 2 a) shows the temporal evolution of the droplet spreading front  $x_{tip}$ , measured as half of the distance between the left and right tips of the droplet, which are marked in Fig. 1, for seven experiments go-

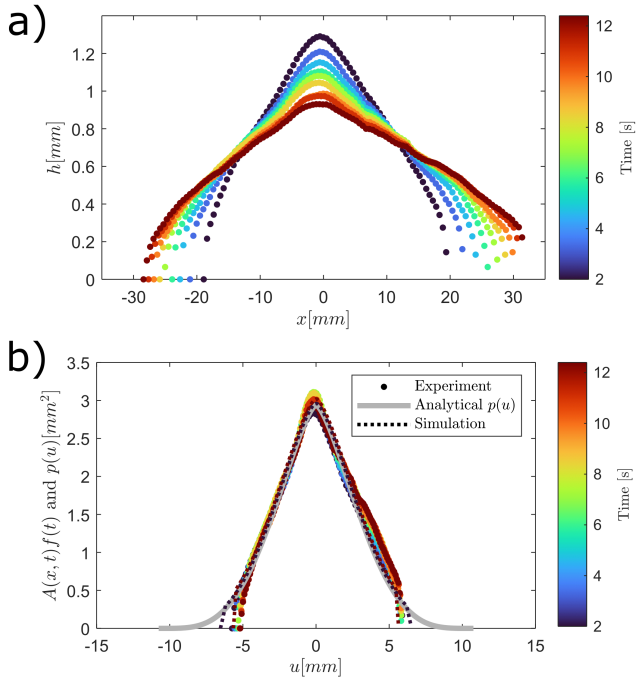


Figure 3: a) Droplet profiles for the experiment with XG concentration of 2 g/l for 9 different times in the range  $t = 2.0$ - $12.4$  s shown in the colorbar. b) The dots show the experimental values of  $A(x, t)f(t)$ . The analytical result for the function  $p(u)$  of Eq. (15) using the value  $n = 0.48$  obtained from Fig. 2 is plotted as a gray line, while the simulations that take the finite corner curvature  $h_0 = 0.6$  mm and initial profile width  $w_0 = 0.8$  mm, are shown for the initial and final times. The diffusion constant resulting from the data fit is  $D_0 = 200 \text{ mm}^{1/n}/\text{s}^1$ .

ing from the Newtonian case (leftmost curve) to the most shear-thinning case (rightmost curve). The linear range in the  $x_{tip}$ -plot allows the determination of  $\tau$  by use of Eq. (16). Fig. 2 b) shows a comparison between the measured  $\tau$ -values against their theoretical predictions. The experimentally and numerically measured exponents are denoted  $\tau_{exp}$  and  $\tau_c$ , and the theoretical values  $\tau_{th}$  are computed from Eq. (12).

We notice that the experimental data tends to gather under the one-to-one  $\tau_{th}$ -line. We attribute this divergence to the fact that in the experimental setup we do not have a sharp wedge. However, the numerically estimated exponents for which this finite curvature radius  $h_0$  is taken into account, agree with the experimental measurements from Fig. 2b) within the error bar in these data except for the smallest and largest  $\tau$ -values. The discrepancy at the largest  $\tau$ -value is most likely caused by inertial effects as the Reynolds number based on the length  $h(0, t)$ , becomes larger than unity for the least viscous, Newtonian fluid. On the other hand, the discrepancy at the smallest  $\tau$ -value is likely caused by a departure from

the non-Newtonian domain, that happens at sufficiently small shear rates. In the Supplementary Material, we show how the numerical  $\tau$ -values depend on  $h_0$  and converges to the analytical result as  $h_0 \rightarrow 0$ . Variations of the initial width  $w_0$  in the 0-2 mm range has less than a 1 % effect on the  $\tau$ -values as initial Gaussian profiles converge quickly to the profiles of Eq. (15) (see Supplementary Material).

Fig. 3 a) shows the experimental profiles  $h(x, t)$  for the spreading of a drop at a XG-concentration of 2g/l and  $V_0 = 19 \text{ mm}^3$ , while Fig. 3 b) shows the data collapse implied by Eqs. 8 and 9 outside the domain where the corner curvature introduces a cut-off. The numerical results capture this behavior, while also showing a close agreement between the analytic and numerical results in the central region. Note that the collapse also verifies the scaling  $x_{tip} \propto t^\tau$  while the agreement between the analytic and numerical results implies a very fast relaxation of the latter to the former.

For the experimental determination of the cross-sectional area  $A(x, t)$  employed in Fig. 3 b), a correction due to the curvature radius  $h_0$  along the corner of the wedge is used so that the normalization  $\int dx A(x, t) = V_0$  is verified. This is done by subtracting from the approximately triangular cross section of the ideal wedge a smaller triangular segment corresponding to the empty segment under the curved segment, see Fig. 1 b). This correction is further described in the Supplementary Material.

## 4 Discussion and conclusions

Having shown that the spontaneous spreading of a power law liquid droplet in a wedge is governed by a non-linear diffusion equation yielding sub-diffusive behavior, we have proceeded via an analytic solution of this equation to obtain the rheological exponents of several power law liquids by simple experimental measurements. The connection between the anomalous diffusion exponent and the fluid rheology expressed in Eq. (12) is the theoretical basis for these experiments. Carrying out the experiments for a range of different liquids we have observed robust behavior in the sense that experimental artifacts like inertial effects, gravity, corner curvature, pinning effects, variability in the contact angle, and finally the crossover to Newtonian behavior at small shear rates, do not dominate in the end the measurements of the rheological exponent.

## Acknowledgments

We thank Alex Hansen and Erika Eiser for helpful discussions along the execution of this project. This

work was partly supported by the Research Council of Norway through its projects 262644 (Center of Excellence funding scheme), 324555 (Researcher Project for Young Talent) and 301138 (NANO2021 program).

## References

- [1] E. Steudle and C. A. Peterson, “How does water get through roots?,” *Journal of Experimental Botany*, vol. 49, p. 775–788, May 1998.
- [2] B. Jamtveit and P. Meakin, eds., *Growth, Dissolution and Pattern Formation in Geosystems*. Dordrecht: Kluwer, 1999.
- [3] M. Tuller, D. Or, and L. M. Dudley, “Adsorption and capillary condensation in porous media: Liquid retention and interfacial configurations in angular pores,” *Water Resources Research*, vol. 35, no. 7, pp. 1949–1964, 1999.
- [4] P. Meakin and A. M. Tartakovsky, “Modeling and simulation of pore-scale multiphase fluid flow and reactive transport in fractured and porous media,” *Reviews of Geophysics*, vol. 47, no. 3, 2009.
- [5] P. Concus and R. Finn, “On the behavior of a capillary surface in a wedge,” *Proceedings of the National Academy of Sciences*, vol. 63, no. 2, pp. 292–299, 1969.
- [6] A. Carlson, G. Bellani, and G. Amberg, “Universality in dynamic wetting dominated by contact-line friction,” *Phys. Rev. E*, vol. 85, p. 045302, 2012.
- [7] P. G. de Gennes, “Wetting: statics and dynamics,” *Rev. Mod. Phys.*, vol. 57, pp. 827–863, Jul 1985.
- [8] J. Van Hulle and N. Vandewalle, “Effect of groove curvature on droplet spreading,” *Soft Matter*, vol. 19, pp. 4669–4675, 2023.
- [9] J. H. Snoeijer and B. Andreotti, “Moving contact lines: Scales, regimes, and dynamical transitions,” *Annual Review of Fluid Mechanics*, vol. 45, no. Volume 45, 2013, pp. 269–292, 2013.
- [10] F. Irgens, *Rheology and Non-Newtonian Fluids*. Cham, Switzerland: Springer International Publishing, Aug. 2016.
- [11] E. Bingham, *An Investigation of the Laws of Plastic Flow*. No. 278 in Bulletin of the Bureau of Standards, U.S. Government Printing Office, 1917.
- [12] P. Coussot, “Saffman–Taylor instability in yield-stress fluids,” *J. Fluid Mech.*, vol. 380, pp. 363–376, Feb. 1999.
- [13] W. R. Schowalter, *Mechanics of non-Newtonian fluids*. London, England: Pergamon Press, Sept. 1978.
- [14] D. R. Heldman, D. B. Lund, and C. M. Sabliov, *Handbook of food engineering*. Boca Raton, FL: CRC Press, 3 ed., Jan. 2019.
- [15] T. Benezech and J. F. Maingonnat, “Characterization of the rheological properties of yoghurt—a review,” *J. Food Eng.*, vol. 21, pp. 447–472, Jan. 1994.
- [16] P. Bertsch, L. Savorani, and P. Fischer, “Rheology of swiss cheese fondue,” *ACS Omega*, vol. 4, p. 1103–1109, Jan. 2019.
- [17] J.-P. Bouchaud and A. Georges, “Anomalous diffusion in disordered media: statistical mechanisms, models and physical applications,” *Elsevier Physics Reports*, vol. 195, pp. 127–293, November 1990.
- [18] E. G. Flekkøy, A. Hansen, and B. Baldelli, “Hyperballistic superdiffusion and explosive solutions to the non-linear diffusion equation,” *Frontiers in Physics*, vol. 9, p. 41, 2021.
- [19] S. Gorthi, S. Meher, G. Biswas, and P. Mondal, “Capillary imbibition of non-newtonian fluids in a microfluidic channel: analysis and experiments,” *Proceedings of the Royal Society A: Mathematical, Physical and Engineering Sciences*, vol. 476, 10 2020.
- [20] R. Pattle, “Diffusion from an instantaneous point source with a concentration-dependent coefficient,” *Mechanics Appl. Math.*, vol. 12, pp. 407–409, 1959.
- [21] M. Tuller and D. Or, “Hydraulic conductivity of variably saturated porous media: Film and corner flow in angular pore space,” *Water Resources Research*, vol. 37, pp. 1257–1276, 5 2001.
- [22] F. Hoogland, P. Lehmann, R. Mokso, and D. Or, “Drainage mechanisms in porous media: From piston-like invasion to formation of corner flow networks,” *Water Resources Research*, vol. 52, no. 11, pp. 8413–8436, 2016.
- [23] M. Moura, E. G. Flekkøy, K. J. Måløy, G. Schäfer, and R. Toussaint, “Connectivity enhancement due to film flow in porous media,” *Physical Review Fluids*, vol. 4, no. 9, p. 094102, 2019.



- [24] P. Reis, M. Moura, G. Linga, P. A. Rikvold, R. Toussaint, E. G. Flekkøy, and K. J. Måløy, “A simplified pore-scale model for slow drainage including film-flow effects,” *Advances in Water Resources*, vol. 182, p. 104580, 2023.
- [25] J. G. Savins, “Non-newtonian flow through porous media,” *Industrial & Engineering Chemistry*, vol. 61, p. 18–47, Oct. 1969.
- [26] W. J. Cannella, C. Huh, and R. S. Seright, “Prediction of xanthan rheology in porous media,” in *All Days*, 88SPE, SPE, Oct. 1988.
- [27] T. Sochi and M. J. Blunt, “Pore-scale network modeling of ellis and Herschel–Bulkley fluids,” *J. Pet. Sci. Eng.*, vol. 60, pp. 105–124, Feb. 2008.
- [28] U. Eberhard, H. J. Seybold, E. Secchi, J. Jiménez-Martínez, P. A. Rühls, A. Ofner, J. S. Andrade, Jr, and M. Holzner, “Mapping the local viscosity of non-newtonian fluids flowing through disordered porous structures,” *Sci. Rep.*, vol. 10, p. 11733, July 2020.
- [29] N. M. Lima, J. Avendaño, and M. S. Carvalho, “Effect of viscoelasticity on oil displacement in a microfluidic porous medium,” *J. Braz. Soc. Mech. Sci. Eng.*, vol. 44, Apr. 2022.
- [30] F. Lanza, A. Rosso, L. Talon, and A. Hansen, “Non-newtonian rheology in a capillary tube with varying radius,” *Transport in Porous Media*, vol. 145, p. 245–269, Aug. 2022.
- [31] S. An, M. Sahimi, T. Shende, M. Babaei, and V. Niasar, “Enhanced thermal fingering in a shear-thinning fluid flow through porous media: Dynamic pore network modeling,” *Physics of Fluids*, vol. 34, Feb. 2022.
- [32] H. Fyhn, S. Sinha, and A. Hansen, “Effective rheology of immiscible two-phase flow in porous media consisting of random mixtures of grains having two types of wetting properties,” *Frontiers in Physics*, vol. 11, June 2023.
- [33] L. Zhang, Z. Yang, Y. Méheust, I. Neuweiler, R. Hu, and Y. Chen, “Displacement patterns of a newtonian fluid by a shear-thinning fluid in a rough fracture,” *Water Resources Research*, vol. 59, Sept. 2023.
- [34] See Supplemental Material at [URL will be inserted by publisher] for additional details on the experimental methods, numerical model and the modification of Darcy’s law for a power-law fluid. The Supplemental Material includes Refs. [13, 40–43].
- [35] A. P. Deshpande, J. M. Krishnan, and P. B. S. Kumar, eds., *Rheology of Complex Fluids*. New York: Springer, 2010.
- [36] S. Ansari, M. A. I. Rashid, P. R. Waghmare, and D. S. Nobes, “Measurement of the flow behavior index of newtonian and shear-thinning fluids via analysis of the flow velocity characteristics in a mini-channel,” *SN Appl. Sciences*, vol. 2, p. 1787, 2020.
- [37] R. L. Hoffman, “A study of the advancing interface. i. interface shape in liquid–gas systems,” *J. Colloid Interface Sci.*, vol. 50, p. 228, 1975.
- [38] P. Sheng and M. Zhou, “Immiscible-fluid displacement: Contact-line dynamics and the velocity-dependent capillary pressure,” *Phys. Rev. A*, vol. 45, p. 5694, 1992.
- [39] M. Latva-Kokko and D. H. Rothman, “Scaling of dynamic contact angles in a lattice-boltzmann model,” *Phys. rev. Lett.*, vol. 98, p. 254503, 2007.
- [40] S. H. Tan, N.-T. Nguyen, Y. C. Chua, and T. G. Kang, “Oxygen plasma treatment for reducing hydrophobicity of a sealed polydimethylsiloxane microchannel,” *Biomicrofluidics*, vol. 4, no. 3, 2010.
- [41] P. J. Whitcomb and C. W. Macosko, *Rheology of Xanthan Gum Solutions*, p. 160–173. American Chemical Society, June 1977.
- [42] G. Phillips and P. Williams, *Handbook of Hydrocolloids*. Woodhead Publishing Series in Food Science, Technology and Nutrition, Elsevier Science, 2009.
- [43] P. J. Carreau, “Rheological equations from molecular network theories,” *Transactions of the Society of Rheology*, vol. 16, p. 99–127, Mar. 1972.

# Supplementary Material for the paper “Anomalous Dynamics of a Liquid Corner Film” by Moura et al.

## A Experimental Methods

### A.1 Preparation of the wedge, polymeric coating and plasma treatment

The key challenge in the preparation of the experiment is ensuring that any types of perturbations to the droplet spreading are minimized. The typical main source of perturbation is contact line pinning, that may arise from either chemical or mechanical heterogeneities in the solid surface of the plates. To reduce contact line pinning, we applied a hydrophilic polymeric coating to the inner surfaces of the plates, followed by low-pressure plasma treatment. The coating was created using the two-part PDMS (Polydimethylsiloxane) Dow SYLGARD 184, a silicone elastomer widely used in microfluidics. The PDMS consists of a base and a curing agent, but because it is naturally hydrophobic, we added a third component, methyl-terminated poly(dimethylsiloxane-b-ethylene oxide) from Polysciences Inc., to act as a hydrophilic agent. We targeted weight ratios of 10:1:0.2 for the base, curing agent, and hydrophilic agent, respectively, with the hydrophilic agent incorporated while the silicone was still fluid, before curing. The mixture was stirred vigorously for several minutes, then placed in a vacuum chamber to eliminate air bubbles introduced during stirring.

While the coating solution was degassing, we prepared the glass plates by positioning them side by side along their longest edge (76 mm). We connected the plates with a strip of Scotch tape acting as a hinge along the edge (see Fig. 1 b). Care was taken to avoid trapping air bubbles, especially along the central edge where droplet spreading occurs.

Next, we used a Laurell WS-650-23B spin coater to apply the coating solution to the glass slides. We added the degassed PDMS solution to the central part of the plates and spun them at 3000 RPM for 2 minutes, following a brief fast acceleration phase. The spinning was repeated once again to ensure a homogeneous thin layer of the modified PDMS solution. The sample was weighed before and after coating, revealing that approximately 0.09 g of PDMS had been deposited, corresponding to a layer thickness of about 0.05 mm. For reference, the thickness of the Scotch tape beneath the PDMS was estimated at 0.03 mm, and the glass plates themselves were 1.0 mm thick.

After coating, the sample was cured in an oven at  $100^{\circ}\text{C}$  for 1 hour. Once the PDMS was fully cured,

we proceeded with the nitrogen plasma treatment. We used a low-pressure plasma system from Diener Electronic for this step. The sample was placed in a sealed plasma chamber, and a vacuum pump reduced the air pressure to 0.15 mbar. A steady nitrogen flow was established to create a nitrogen-rich environment at 0.3 mbar. Plasma was then activated and maintained at 60% power for 3 minutes.

This plasma treatment was crucial for achieving hydrophilicity, as the hydrophilic agent alone was insufficient. PDMS is inherently hydrophobic, with a water-air contact angle around  $\Theta = 120^{\circ}$  [40]. Before plasma treatment, we measured a contact angle of  $\Theta = 75^{\circ}$  using a droplet of xanthan gum solution (2 g/l in water). After plasma treatment, the contact angle decreased to approximately  $\Theta = 20^{\circ}$ .

### A.2 Preparation of the fluids

The power-law fluids were prepared by mixing different concentrations of xanthan gum in water using a magnetic stirrer. As noted by Whitcomb [41] adding just 1% xanthan gum to water can enhance its viscosity up to 100 000 times at low shear rates, but this increase was limited to only 10 times at high shear rates. We start the procedure by adding 250 g of deionized water in a container that is placed in a magnetic stirrer at a rate high enough to form a visible vortex. The XG is gradually poured onto the side walls of the generated vortex in order to avoid the formation of large clumps. After 1 h we added 0.25 g of Nigrosin, a strong dark blue water-soluble dye. We also prepared a reference Newtonian fluid by simply mixing glycerol and water, 50% by weight of each part.

After mixing, microscopic air bubbles were inevitably trapped in the fluids, potentially affecting their rheology. To address this, the fluids were placed in a vacuum chamber for degassing.

### A.3 Rheological measurements using a commercial rheometer

The rheology of all fluids was characterized using an Anton Paar rheometer model MCR 702e. We performed tests in which the shear rate  $\dot{\gamma}$  increased gradually from  $\dot{\gamma}_{min} = 0.01 \text{ s}^{-1}$  to  $\dot{\gamma}_{max} = 100 \text{ s}^{-1}$  for all XG fluids and from  $\dot{\gamma}_{min} = 1 \text{ s}^{-1}$  to  $\dot{\gamma}_{max} = 10 \text{ s}^{-1}$  for the Newtonian glycerol-water mixture. The results for the effective viscosity  $\mu$  as a function of the



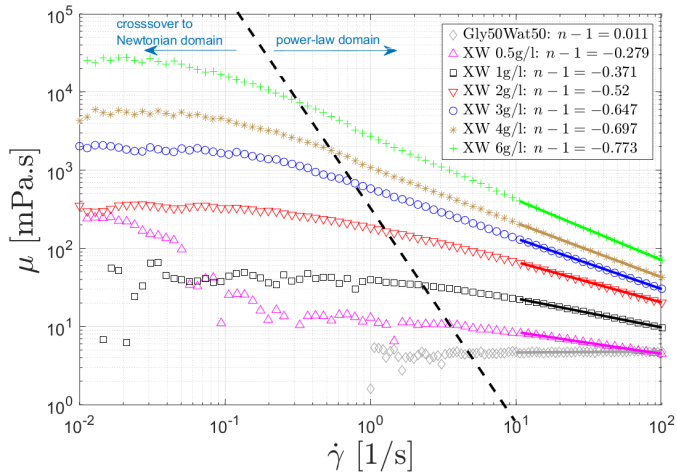


Figure 4: Viscosity curve from the Anton Paar MCR 702e rheometer for the different power-law fluids. The reference Newtonian glycerol-water mixture is also shown. The region used to extract the power-law exponent  $n - 1$  corresponds to the solid lines. The dashed line shows the transition region between the Newtonian and power-law domains, while the full line shows the predictions.

shear rate  $\dot{\gamma}$  are shown in Fig. 4. Note that all fluids present a power-law regime behavior of the form  $\mu \propto \dot{\gamma}^{(n-1)}$  for high values of the shear rate  $\dot{\gamma}$  (shown as solid lines in the figure). The fluids became more shear-thinning for higher concentrations of XG, see the concentration and exponent values in the legend. The power-law regime is only observed beyond some threshold value  $\dot{\gamma}^*$  which depends on the concentration of XG. Increasing the XG concentration causes  $\dot{\gamma}^*$  to decrease. The approximate boundaries between the power-law regime and a crossover regime is shown by the dashed line in the plot. When  $\dot{\gamma} < \dot{\gamma}^*$ , the fluids are in a crossover region and for very small shear rates the fluids present a Newtonian behavior with a constant viscosity. Measurements at extremely high shear rates were not performed however, at such rates, the viscosity of xanthan gum solutions tends to approach that of water [42]. This crossover regime is well documented [13] and was captured in more complex models for the viscosity curve such as that by Carreau [43].

The  $\mu_0$  values at that may be read of from Fig. 4 at  $\dot{\gamma}_0 = 10 \text{ s}^{-1}$  are roughly within a factor 2 of the values obtained from Eq. (17) using the static contact angle. However, if this value is replaced by a dynamic contact angle  $\Theta_{dyn}$ , agreement between the values obtained from Fig. 4 and the prediction of Eq. (17) may be achieved, using  $\Theta_{dyn} \approx \pi/3$  as a fitting parameter. This strongly suggests that while the theoretical exponent  $n$  obtained from the measured  $\tau$ -values, is universal in the sense that it does not depend much

on the idealizations made in the theory, the prefactor  $\mu_0$  does.

In Fig. 4, we also notice that for the samples presenting the lower values of the effective viscosity, the data begins to fluctuate and becomes unreliable for very low shear rates. We believe this happens because in this zone, the torque imposed by the fluid on the rheometer plates is too small to be reliably measured. This can be clearly seen on the curves for XG 0.5g/l where the data start to fluctuate for values below  $\dot{\gamma} = 0.3 \text{ s}^{-1}$  and in the Newtonian case where the fluctuation starts around  $\dot{\gamma} = 3 \text{ s}^{-1}$ . In the analysis in this work, we have focused only on the portion of the curve in the power-law domain.

#### A.4 Droplet placement and effects from films on the plates

A micrometer syringe with a flat-tipped needle is used to deposit a droplet of the specified liquid at the wedge's center. The external diameter of the needle is 1.80 mm and the droplet volume (set on the syringe) is approximately 20 microliters. The micrometric needle is positioned in an arm connected to a translation stage which allowed for  $x$ ,  $y$  and  $z$  translation to position the droplet in the wedge. The procedure of placing one droplet consisted in first generating the pendant droplet on the needle and then slowly moving the translation stage down until the droplet touched the inner sides of the plates. It would then disconnect from the needle and start spreading sideways, see Fig. 1. Notice that once the droplet touches the glass plates, it creates a wetted region close to the center which persists as the experiment progresses. This can be seen on Fig. 1 b) as the darker patch just below the tip of the needle in the central part of the image. The presence of this film can cause the droplet shape for small  $x$  values (close to the center) to deviate from the theoretically predicted shapes where this artifact was not present. The lateral extent of this region is of the order of  $0.3 \text{ cm}$  in both directions so in our analysis we have ignored the initial frames of the dynamics in which the droplet spreading may be more affected by these films.

#### A.5 Experiments with highly wetting silicone oils using a simpler wedge construction

For highly wetting liquids, such as silicone oils, contact line pinning is naturally reduced and a simpler setup with only the glass wedge without any polymeric coating or plasma treatment is sufficient. As a first step in the development of our technique, We performed experiments with this simpler wedge con-

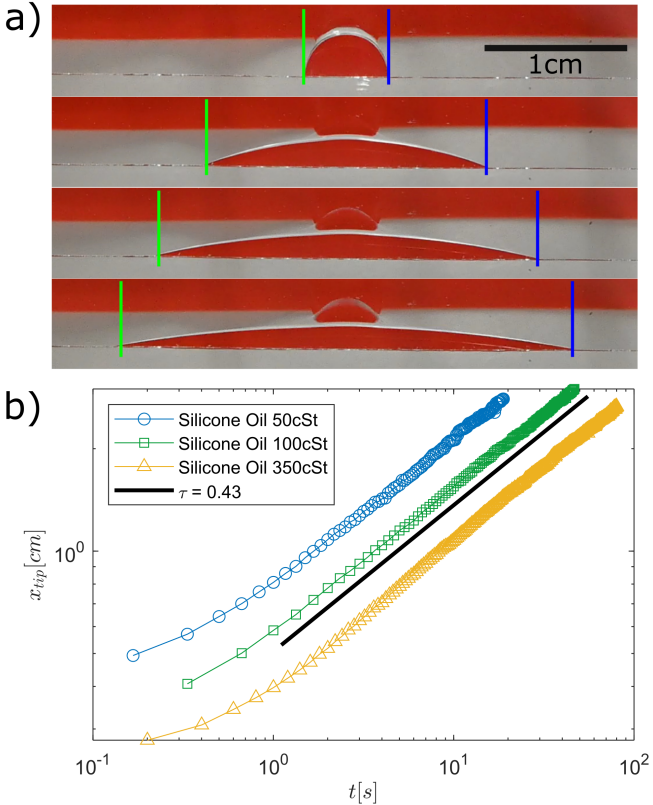


Figure 5: a) Snapshots showing the evolution of a droplet of highly wetting silicone oil with a viscosity 100 cSt in the wedge composed only of two glass slides. The interval between the top and bottom snapshots is  $\Delta t = 10$  s. b) The spreading dynamics of three silicone oils with viscosities 50 cSt, 100 cSt and 350 cSt show similar exponents  $\tau = 0.43 \pm 0.03$ , (black line). The data is shifted horizontally by different values to aid visualization.

struction using silicone oils with kinematic viscosities 50 cSt, 100 cSt and 350 cSt. In Fig. 5 we shows snapshots of the experiment with the 100 cSt silicone oil. The transparent silicon oil appears red because of a convenient lensing effect: A red tape is positioned behind the wedge and the contrast in refracting indices causes the droplet to refract the red light into the camera, thus avoiding the need for dyes. The interval between the first and last snapshots was  $\Delta t = 10$  s. The spreading dynamics is seen in Fig. 5 b) where we see that all exponents show values  $\tau = 0.43 \pm 0.03$  obtained from the black guide-to-the-eye line. These findings are consistent with the fact that silicone oil is a Newtonian fluid with a theoretically value  $\tau = 0.4$ , which results from setting  $n = 1$  in Eq. (12). In this experiment, the wedge had an opening angle of  $\alpha = 20^\circ$ , and the droplet was positioned by hand instead of employing the more precise arrangement with a micrometric syringe. Images were recorded with a DSLR camera in video mode. Notice that even though the fluids are significantly different, with

viscosities varying by a factor of 7, the exponent is rather stable. The specific value of the viscosity, as well as the opening angle  $\alpha$ , enters in the prefactor governing the scaling through the ‘diffusion coefficient’  $D_0$  in Eq. (7) but do not affect the exponent  $\tau$ .

## A.6 Estimation of cross sectional area of droplet from experimental height profile

In the experiments the cross sectional area  $A(x, t)$  is affected by the curvature of the edge as shown schematically in Fig. 1 b). If we ignore this effect, the computed volume of the droplet differs from the known value  $V_0$ , which is injected by the needle. The effective height  $h$  measured experimentally is the vertical distance from the top of the liquid water interface and the curved segment in Fig. 1 b), which itself is at a distance  $\approx h_0$  from the extrapolated, sharp edge of the wedge. We can estimate  $A(x, t)$  then as the difference between the area of the triangular wedge (ideal case with sharp corner) and the void space under the curved segment seen in Fig. 1 b). From a simple geometrical argument we get

$$A \approx (h + h_0)^2 \tan\left(\frac{\alpha}{2}\right) - h_0^2 \tan\left(\frac{\alpha}{2}\right) = (h^2 + 2hh_0) \tan\left(\frac{\alpha}{2}\right). \quad (18)$$

The vertically projected effective height  $h$  is what is shown in Fig. 3 a). Notice that this is slightly different from  $h$  seen in Fig. 1 but can be obtained from the latter as  $h \cos(\alpha/2) - h_0$ .

## B Numerical model

In Fig. 6 the droplet height  $h(x, t) = \sqrt{2A(x, t)/\alpha}$  is plotted as a function of position, where we have taken the normalization to be  $\int dx A(x, t) = 19 \text{ mm}^3$ , approximating the experimental value. Note that the analytic solution (red and green curves for times given in the legend) has a cusp at  $x = 0$  where the second spatial derivative of  $h(x, t)$  diverges, while the numerical solution is initialized with the smooth Gaussian  $\propto \exp(-x^2/w_0^2)$  (shown as the taller curve). Nevertheless, the numerical solution converges to the analytical solution (red curve) with the same droplet volume within 1 % during the first 1/10 of the time span, except at the cut-off point  $h \approx h_0$ , where a weak numerical oscillation around the analytic solutions causes deviations of the order 1 %. This shows that the numerical solution quickly converges to the analytical shape prediction, except for the values where  $h$  is below the  $h_0$ -cutoff. Fig. 7 shows that  $x_{tip}(t)$

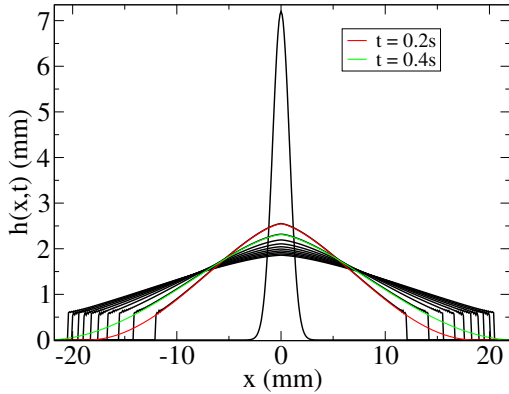


Figure 6: The film height as a function of position along the corner at different times when the rheological exponent  $n = 0.48$ . The black lines derive from the numerical solutions of Eq. (6) using  $h(x, t) = \sqrt{2A(x, t)/\alpha}$ , while the colored line shows the corresponding analytical solution of Eq. (8) and Eq. (15) for two different times. The taller central curve shows the initial profile of the droplet. A volume of  $19 \text{ mm}^3$ , initial width  $w_0 = 0.8 \text{ mm}$  and corner radius of  $h_0 = 0.6 \text{ mm}$  were used as parameters for the simulated curves.

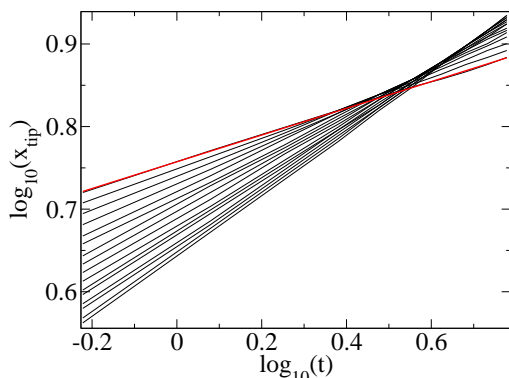


Figure 7: The position of the right droplet tip as a function of time for  $n$ -values in the range 0.25-1.0 (black curves). The red curve is a linear fit to the black  $n = 0.25$  curve, which it nearly covers. All other parameters are as in Fig. 6.

when  $h_0 = 0.6 \text{ mm}$  and  $w = 0.8 \text{ mm}$ , is very well approximated by a powerlaw, that is, that it yields straight lines on a log-log plot. The deviation from the theoretical  $\tau$  value (shown by the red dot) decreases with decreasing  $h_0$ , as expected. In Fig. 8 the slopes of these plots are given, showing the variation of  $\tau_c$  with the corner curvature  $h_0$ . Note that they extrapolate well to the analytic value given by the red dot.

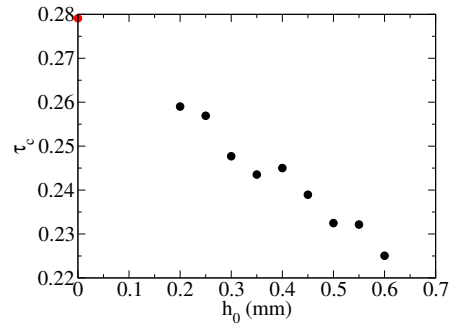


Figure 8: The measured slopes  $\tau_c$  derived from the numerical solution of Eq. (6) versus the radius of curvature of the corner  $h_0$ . Here  $n = 0.48$  and the red dot shows the theoretical value given in Eq. (12).

## C Replacement of Darcys law for a power-law fluid

We need the relationship between the pressure gradient and the average flow velocity of a power-law fluid where the viscous stress  $\propto \dot{\gamma}^n$ , the shear rate and  $n$  the rheological exponent, which for a shear-thinning fluid is smaller than unity. When  $n = 1$  the fluid is Newtonian. Just as the viscous stress in a Newtonian fluid, the non-Newtonian fluid stress tensor can only depend on the symmetric part of the velocity gradient. For an incompressible fluid the total stress tensor, which includes the pressure  $P$ , may be cast in the covariant form

$$\sigma_{tot\ ij} = -\delta_{ij}P + \eta_0 \dot{\gamma}_{ij} (\dot{\gamma}_{kl} \dot{\gamma}_{kl})^{(n-1)/2} \quad (19)$$

where  $P$  is the pressure,  $\delta_{ij}$  the Kronecker delta function and summation over repeated indices is implied. The viscosity coefficient (in units of  $\text{Pa s}^n$ ) may be decomposed into  $\eta_0 = \mu_0 \dot{\gamma}_0^{1-n} = \mu$ , where  $\mu_0$  (in units of  $\text{Pa s}$ ) is the viscosity at the shear rate  $\dot{\gamma}_0$ . The strain rate tensor

$$\dot{\gamma}_{ij} = \frac{\partial u_i}{\partial x_j} + \frac{\partial u_j}{\partial x_i}. \quad (20)$$

The stress balance equation is

$$\nabla \cdot \sigma_{tot} = 0. \quad (21)$$

When  $n = 1$ , this equation reduces to the Stokes equation.

Introducing a characteristic length  $h$ , which could be the channel width, this equation may be written in terms of the non-dimensional primed quantities defined through

$$\begin{aligned} x_i &= hx'_i \\ u_i &= \dot{\gamma}_0 h u'_i \\ \dot{\gamma}_{ij} &= \dot{\gamma}_0 \dot{\gamma}'_{ij} \\ \nabla &= \frac{1}{h} \nabla'. \end{aligned} \quad (22)$$

Writing the pressure gradient as

$$\nabla P = -g\mathbf{e} \quad (23)$$

where  $\mathbf{e}$  is the unit vector in the opposite direction of the pressure gradient, Eq. (21) may be written as

$$\mathbf{e} = -\nabla' \cdot \left( \dot{\gamma}'' (\dot{\gamma}''^2)^{(n-1)/2} \right) \quad (24)$$

where  $\gamma'' = \gamma'/G^{1/n}$  and we have introduced the dimensionless ratio between pressure forces and viscous forces, and

$$G = \frac{gh}{\mu_0 \dot{\gamma}_0} \quad (25)$$

which is thus a non-dimensionalized pressure gradient. Since the boundary conditions may be given in terms of  $\mathbf{u}'(\mathbf{x}'_B)$  where  $\mathbf{x}'_B$  are boundary coordinates, the stress balance equation yields a solution of the form

$$\gamma''_{ij} = f_{ij}(\mathbf{x}') \quad (26)$$

which in turn gives

$$\gamma'_{ij} = f_{ij}(\mathbf{x}') G^{1/n} \sim \frac{\partial u'_i}{\partial x'_j}. \quad (27)$$

Integrating this equation gives

$$u' = G^{1/n} F_i(\mathbf{x}'), \quad (28)$$

for some other dimensionless function  $\mathbf{F}_n$ , which in turn gives

$$u = G^{1/n} \dot{\gamma}_0 h F_n(\mathbf{x}'). \quad (29)$$

Averaging over a cross-section of the flow gives

$$\bar{u} = G^{1/n} \dot{\gamma}_0 h Q = \left( \frac{g}{\eta_0} \right)^{1/n} h^{1+1/n} Q_n. \quad (30)$$

It is possible to calculate  $Q_n$  in the lubrication approximation, assuming that the flow is governed by the gradients of  $u$  in the angular direction (normal to the wedge walls) alone.

We shall start with the velocity field  $u(x)$  in the  $z$ -direction in a straight channel of half-width  $a$  and a coordinate  $x$  in the direction transverse to the flow where  $x = 0$  in the middle. The velocity satisfies the boundary condition  $u(\pm a) = 0$ . Then Eq. (21) reduces to

$$2^{\frac{1-n}{2}} \frac{g}{\eta_0} - \partial_x ((-\partial_x u)^n) = 0, \quad (31)$$

for  $x > 0$ . This equation is easily integrated to yield

$$u(x) = 2^{\frac{1-n}{2n}} \frac{n}{n+1} \left( \frac{g}{\eta_0} \right)^{1/n} \left( a^{\frac{n+1}{n}} - x^{\frac{n+1}{n}} \right), \quad (32)$$

which has the cross-sectional average

$$\bar{u} = \frac{1}{a} \int_0^a dx u(x) = 2^{\frac{1-n}{2n}} \frac{n}{2n+1} \left( \frac{g}{\eta_0} \right)^{1/n} a^{\frac{n+1}{n}}. \quad (33)$$

This expression is seen to agree with Darcys law in a channel of half-width  $h$  in the Newtonian  $n = 1$  case where  $\bar{u} = h^2 g / (3\eta_0)$ .

Now, returning to the wedge-geometry, we replace  $a \rightarrow \alpha r/2$ , thereby obtaining a lubrication approximation  $\bar{u}(r)$  to this flow at a distance  $r$  to the corner. This approximation is expected to work well for small  $\alpha$ . Averaging  $\bar{u}(r)$  over the cross-sectional area

$$\langle u \rangle = \frac{2}{h^2} \int_0^h dr r \bar{u}(r) \quad (34)$$

yields the volume flux

$$q = \frac{\alpha h^2}{2} \langle u \rangle = Q_n \left( \frac{g}{\eta_0} \right)^{1/n} h^{3+1/n} \quad (35)$$

where

$$Q_n = \frac{2^{\frac{1+n}{2n}} n^2}{(2n+1)(3n+1)} \left( \frac{\alpha}{2} \right)^{\frac{2n+1}{n}}, \quad (36)$$

which is the desired result.